High-content assay for precision medicine discovery in cystic fibrosis.

Stella Prins[1], Emily Langron[1], Cato Hastings[2], Emily J. Hill[1], Andra C. Stefan[3], Lewis D. Griffin[2] and Paola Vergani[1]*

[1] Department of Neuroscience, Physiology and Pharmacology

[2] CoMPLEX

[3] Natural Sciences

University College London

Gower Street

WC1E 6BT London UK

The first two authors contributed equally to this project.

*Correspondence to: p.vergani@ucl.ac.uk

Keywords: CFTR, protein transport, ion channels, VX-770, fluorescence imaging.

Bullet point summary

What is already known:

- CFTR is an anion-selective channel, normally present in the plasma membrane of epithelial cells.
- Hundreds of different mutations affect CFTR biogenesis and/or function causing cystic fibrosis (CF).

What this study adds:

- We present and validate an assay that simultaneously measures CFTR biogenesis and function.
- Profiling a panel of CF-causing mutants suggests hypotheses on how approved drug VX-770 works.

Clinical Significance:

- The integrated assay boosts potential for discovery of more effective therapies, simultaneously repairing both defects.

Abstract

Background and Purpose: Cystic fibrosis (CF) is a life-limiting disease caused by mutations in the human *CFTR* gene, encoding an anion-selective channel. Because CF-causing mutations affect both CFTR permeation/gating and biogenesis, multi-assay approaches have been implemented in drug development, sequentially screening for channel function and membrane density. Here we present the first assay capable of simultaneous assessment of both CFTR characteristics.

Experimental approach: Images of live HEK293 cells co-expressing a soluble and a CFTR-tagged fluorescent protein are automatically acquired and analysed to quantify both CFTR membrane density and ion channel function. We monitor F508del-CFTR, the most common disease-causing mutant. Furthermore we characterize a panel of 62 CF-causing mutations and profile effects of acute treatment with approved drug VX-770, mapping potentiation on CFTR structures.

Key Results: We validate our assay by confirming F508del-CFTR rescue by incubation at low temperature, treatment with CFTR-targeting drugs and introduction of second-site revertant mutation R1070W. Measurements using the rare mutations panel also correlate well with published results.

Conclusions and Implications: Mapping of VX-770 potentiation of mutants suggests that by increasing flexibility around the gate, the drug allows an alternative protein conformation at domain interfaces around site 1.

The assay is a powerful tool for investigation of CFTR ion channel biophysics, allowing more accurate inferences on gating/permeation properties than can be obtained by measuring cellular conductance alone. Finally, by providing a two-dimensional molecular characterization of individual mutant CFTR proteins, our assay can better inform development of single-drug and combination therapies addressing the root cause of CF disease.

Abbreviations

ABC	ATP-binding cassette
CF	Cystic Fibrosis
CFTR	Cystic Fibrosis Transmembrane Conductance Regulator
$F_{\text{YFP membrane}}$	average normalized YFP fluorescence intensity within the membrane zone
$F_{\text{mCherry cell}}$	average normalized mCherry fluorescence over the entire cell
G_{CFTR}	CFTR conductance
G_{trans}	transient anion conductance
IRES	internal ribosome entry site
NBD	nucleotide binding domain
PDL	poly-D-lysine
P_O	open probability
ρ	CFTR membrane density
SSR	sum of squared residuals
τ_{trans}	time constant of the transient anion conductance
V_M	membrane potential
WT	wild type
YFP	yellow fluorescent protein

Introduction

Cystic fibrosis (CF) is a life-limiting genetic disease most prevalent in people with a Caucasian background. Although the median survival age has increased by almost 12 years over the last decade, the disease strongly impacts expectation and quality of life (Elborn, 2016).

CF is caused by mutations in the *CFTR* gene (Riordan et al., 1989; Rommens et al., 1989), encoding an anion-selective channel (Csanády et al., 2019) present on the apical plasma membrane of epithelial cells. These mutations decrease the density of CFTR channels located on the cell membrane (by affecting protein synthesis, folding, intracellular trafficking, plasma membrane stability), and/or impair channel function (impacting on gating or anion permeation). As a result, transepithelial fluid movement is abnormal, creating problems particularly affecting lungs, pancreas, intestines, liver and reproductive systems.

Engineering of a halide sensitive YFP with increased affinity for iodide and a low affinity for chloride (Galietta et al., 2001a; Galietta et al., 2001b), allowed the first high throughput screening projects, which assessed CFTR activity by measuring the rate of YFP quenching caused by iodide influx and chloride efflux(Ma et al., 2002; Pedemonte et al., 2005a; Pedemonte et al., 2005b; Yang et al., 2003). Later, Vertex Pharmaceuticals used changes in membrane potential, monitored through fluorescence resonance energy transfer, to indirectly quantify CFTR channel function (Van Goor et al., 2009; Van Goor et al., 2006).

These efforts led to the identification of the first CFTR modulator drugs, directly targeting the defective CFTR protein. Modulators have been classified as either “potentiators”, increasing CFTR channel function, or “correctors” increasing the number of CFTR channels on the plasma membrane. The potentiator ivacaftor (VX-770) (Van Goor et al., 2009) is now approved for the treatment of patients carrying the G551D gating mutation and a number of other mutations impairing channel function (Gentzsch & Mall, 2018). However, neither potentiation by VX-770 on its own (Flume et al., 2012), nor treatment with the corrector VX-809 (Van Goor et al., 2011) alone (Clancy et al., 2012), significantly improves lung function of patients homozygous for the F508del mutation, present on at least one allele in ~90% of patients. Like many other CF-causing mutations, F508del results not only in ion channel dysfunction, but also in a reduction of the number of channels present at the cell surface. Combination treatment with VX-770 and VX-809 provides small but significant health benefits (Wainwright et al., 2015). Triple combination therapies, combining two different correctors with a potentiator, hold promise to further improve patient outcomes (Davies et al., 2018; Keating et al., 2018).

More than 300 CF-causing mutations have been characterized (The Clinical and Functional TRanslation of CFTR (CFTR2); available at http://cftr2.org). Each mutation, other than F508del, is extremely rare, and is likely to affect the folding, trafficking, stability, gating dynamics and/or permeation of the encoded CFTR protein differently. Pre-clinical data informing on how drugs affect individual CFTR variants in simplified *in vitro* systems, is thus very valuable for drug development and trial design.

Here we present a medium-throughput image-based assay that acquires multi-dimensional data (dual-colour fluorescence intensity in time and space) on individual live HEK293 cells and extracts information on two key characteristics of CFTR. By co-expressing soluble mCherry with the halide sensitive YFP (Galietta et al., 2001a) linked to CFTR (Langron et al., 2017), our new assay gives readouts of both CFTR function, and CFTR membrane density. Experimental manipulation - incubation at low temperature (Denning et al., 1992; Rennolds et al., 2008; Wang et al., 2008), treatment with VX-809 (He et al., 2013; Okiyoneda et al., 2013) with and without VX-770 (Cholon et al., 2014; Veit et al., 2014), and addition of revertant mutation R1070W (Farinha et al., 2013; Okiyoneda et al., 2013; Thibodeau et al., 2010) - results in the expected changes in measured F508del-CFTR channel function and membrane density. Furthermore, we present a screening platform suitable for profiling the molecular characteristics of 62 CFTR variants carried by CF patients. Profiling the effects of VX-770 (Vertex Pharmaceuticals) on this panel validates our new assay as a powerful tool for "high-content" CFTR monitoring in pharmacological research.

Results

The assay

To obtain quantitative information about ion channel function of CFTR, we exploited a halide-sensitive YFP (Galietta et al., 2001a; Galietta et al., 2001b), tagged to the N-terminal of CFTR (Langron et al., 2018; Langron et al., 2017). We constructed a pIRES2-mCherry-YFPCFTR plasmid that directs co-expression of YFP(H148Q/I152L)-CFTR (hereafter designated YFP-WT-CFTR or simply WT-CFTR) and a soluble, cytosolic, red fluorescent protein, mCherry (Shaner et al., 2004) (Figure 1A). The mCherry expression allows image segmentation and localization of the cell membrane by marking the border of cells. Furthermore, mCherry serves as an internal standard for the normalisation of YFP-CFTR expression, eliminating variability due to unequal transfection efficiency.

Yellow fluorescence at the boundaries of areas of red fluorescence is used to estimate CFTR membrane density for each cell (Figure 1). The "membrane" is defined as comprising a ~1 μm wide band, on the inside of a cell's boundary. The density of CFTR at the membrane (ρ), is estimated by dividing the average YFP-CFTR fluorescence intensity within the membrane zone ($F_{\text{YFP membrane}}$), by the average mCherry fluorescence over the entire cell ($F_{\text{mCherry cell}}$). The ρ metric can be thought of as the product of the proportion of CFTR localized to the membrane ($F_{\text{YFP membrane}}/F_{\text{YFP cell}}$), multiplied by the metabolic stability of YFP-CFTR with respect to mCherry ($F_{\text{YFP cell}}/F_{\text{mCherry cell}}$). Thus, changes in ρ metric will reflect not only changes in CFTR trafficking, but also changes in the overall rates of biosynthesis vs. degradation of the protein.

Increasing F508del-CFTR membrane density

To validate our assay, we assessed changes in F508del-CFTR membrane density by comparing distributions of $\log_{10}\rho$ (logarithmic transformation of the ρ metric) obtained from thousands of cells for each genotype/condition (Figure 2).

<u>F508del-CFTR: VX-809 incubation</u>

At 37°C, incubation with VX-809 for 24 hours caused a small but significant increase in $\log_{10}\rho$ of F508del-CFTR, (Figure 2A left, see also Supplementary Table S1). At 28°C, the magnitude of the increase was greater (Figure 2A right).

<u>F508del-CFTR: R1070W second-site revertant mutation</u>

Introducing the second-site revertant mutation R1070W (Thibodeau et al., 2010) in the F508del-CFTR background, significantly increased membrane density at 37°C, (Figure 2B left, Supplementary Table S1), as well as at 28°C (Figure 2B right, Supplementary Table S1). Again, the magnitude of the effect was larger at 28°C.

<u>F508del-CFTR: chronic VX-770 incubation</u>

When comparing cells expressing F508del-CFTR incubated for 24 hours with VX-809 alone, with those incubated with both VX-809 and VX-770, at 37°C, there was a small but significant decrease in $\log_{10}\rho$ (Figure 2C left, Supplementary Table S1). At 28°C the decrease was again more pronounced than at 37°C (Figure 2C right).

F508del-CFTR: temperature correction

Because our fluorescence readings are normalized to those obtained from cells expressing WT-CFTR grown on the same 96-well plate, we quantified the difference between the mean $\log_{10}\rho$ of WT-CFTR and F508del-CFTR at each temperature. The $\log_{10}\rho$ values of F508del-CFTR were found to be significantly closer to those of WT-CFTR at 28°C, than at 37°C, (Figure 2D, Supplementary Table S1).

Increasing F508del-CFTR ion channel function

Following addition of extracellular I^- (I^- first Protocol, see Methods), CFTR was activated by 10 µM forskolin alone, or by a combination of 10 µM forskolin and 10 µM VX-770 (the latter defined as an acute (a) treatment, as opposed to the 24-hour chronic (c) incubation with VX-770 described above). The normalized fluorescence of HEK293-cells expressing YFP-tagged WT-CFTR, F508del-CFTR, or F508del/R1070W-CFTRwas followed over time (Figure 3). The maximal rate of I^- entry was used to summarize CFTR channel function for the different CFTR genotypes, incubation and activation conditions tested (Figure 3E, Supplementary Tables S2 and S3). No significant difference in this metric was detected among the different genotypes/conditions when DMSO (vehicle) was added instead of activators .

WT-CFTR

As expected, in cells expressing WT-CFTR, the maximal rate of I^- entry was significantly higher after activation with forskolin, compared to control (DMSO), at both 37°C and 28°C (Figure 3A; Figure 3E WT). However, neither the presence of 10 µM VX-770 in addition to forskolin during activation, nor incubation at 37°C vs. 28°C modified quenching rate sufficiently to achieve statistical significance after multiple comparison correction (Figure 3A; Figure 3E, WT, Supplementary Table S3).

F508del-CFTR: activation following temperature correction

Activation with forskolin alone failed to increase the maximal rate of I^- entry in untreated cells expressing F508del-CFTR (Figure 3B top; Figure 3E F508del bars 1 and 4, Supplementary Table S2), reflecting the severe gating defect which persists even after temperature correction. Acute potentiation by VX-770 was required to detect function of the channels reaching the cell

surface thanks to temperature-correction (Figure 3B, bottom; Figure 3E F508del bars 5 vs. 2, Supplementary Table S2).

F508del-CFTR: activation following VX-809 correction

At both temperatures, the activity of F508del-CFTR channels reaching the cell surface after 24-hour incubation with VX-809 could be detected following acute activation with forskolin and VX-770. At 28°C the maximal rate of I^- entry was significantly greater than at 37°C (Figure 3C; Figure 3E, F508del bar 6 vs. 3, Supplementary Table S3).

F508del-CFTR: rescue of ion channel function by the R1070W mutation

Forskolin activation alone was enough to reveal F508del/R1070W-CFTR channel activity (Figure 3D, Supplementary Table S2). The maximal rate of I^- entry was significantly higher at 28°C than at 37°C (Figure 3D; Figure 3E F508del/R1070W, Supplementary Table S3).

The rare mutation panel

CF-causing missense CFTR mutations (Sosnay et al., 2013; Van Goor et al., 2014; Yu et al., 2012) were individually introduced in the pIRES2-mCherry-YFPCFTR plasmid, creating a panel of 62 plasmids (including WT-CFTR as reference).

Following expression of the panel in HEK293 cells, and incubation with no pharmacological correction, distributions for the ρ metric, and plate $\log_{10}\rho$ means were obtained (Supplementary Table S4, Supplementary Figure S5). The data is summarized in Figure 4A, which profiles membrane density for each CFTR mutant in the panel. Correlation between our measured ρ and the proportion of CFTR acquiring complex glycosylation in FRT cells is surprisingly good (r^2 = 0.65, Sosnay et al., 2013; r^2 = 0.48, Van Goor et al., 2014), considering the differences in expression system and metric used (note that correlation between the two published datasets is r^2 = 0.48).

YFP-CFTR fluorescence quenching experiments (I^- last Protocol, see Methods) were carried out to estimate steady-state CFTR conductance (G_{CFTR}), without (DMSO) and with baseline CFTR activation by 10 µM forskolin (Figure 4B-C; Supplementary Table S6). Again, results correlate well with published data (r^2 = 0.68, Sosnay et al., 2013; r^2 = 0.60 Van Goor et al., 2014). Conductance was also measured in the presence of 10 µM forskolin + 10 µM VX-770 (Figure 4B, D; Supplementary Table S7). In these conditions, genotypes with high

conductance (including WT-CFTR) have faster YFP quenching than can be reliably measured in our system. However, the assay can accurately monitor VX-770 potentiation when CFTR activity is low, as is the case for most mutants (Van Goor et al., 2014).

Relationship between CFTR ion channel function and membrane density

By considering the changes in ion channel function in the context of any changes measured in ρ, our assay allows more accurate inferences on the gating and permeation properties of the CFTR channel molecules present at the cell surface.

Even when virtually no channels are present in the plasma membrane (as happens e.g. for cells expressing F508del-CFTR incubated at 37^0 C) the value of ρ does not fall to zero. This is likely due to some inaccuracy in automated cell boundary detection and to the widefield microscope optics, resulting in stray light from out-of-focus planes reaching the photomultiplier. To empirically investigate the relationship between G_{CFTR} and ρ, cells expressing F508del-CFTR were treated with increasing concentrations of corrector VX-809, progressively improving both biogenesis/membrane stability and conductance (Figure 5A). Measured G_{CFTR} values as a function of ρ values show a roughly linear relationship. The trendline can be extended to cross the ρ axis, extrapolating to an intercept at $\rho = 0.23$. In addition, extension towards higher membrane densities shows how gating of F508del-CFTR, VX-809-corrected and acutely potentiated by VX-770, reaches levels characteristic of WT-CFTR (without potentiation), consistent with patch-clamp open probability (P_O) measurements (Kopeikin et al., 2014; Wang et al., 2018).

Data on maximum rate of I^- entry can also be plotted against the corresponding ρ values, measured for the different F508del-CFTR rescue strategies (Figure 5B). A linear interpolation between data points for uncorrected F508del-CFTR and WT-CFTR activated by 10 μM forskolin describes the ion channel function we would expect from cells with increasing CFTR membrane density, assuming gating and permeation characteristics of baseline-activated WT-CFTR. This allows us to infer how rescued F508del-CFTR channels reaching the membrane compare to control channels in terms of function. The resulting x-axis intercept ($\rho = 0.25$) is very similar to that obtained using G_{CFTR} to quantify ion channel function.

Introducing the R1070W revertant mutation in the F508del-CFTR background is shown to be particularly effective in improving gating. Comparing revertant rescue with temperature correction, Figure 5B shows how both strategies similarly increase membrane density but

temperature-corrected F508del-CFTR channels at the membrane have very low ion channel function (unless acutely potentiated with VX-770). In contrast, F508del/R1070W channels at the membrane have gating and permeation properties equal - or even superior - to WT-CFTR (Figure 5B, cf. F508del/R1070W-CFTR red symbol vs. uncorrected F508del-CFTR blue symbol). Both results are consistent with patch-clamp records indicating a F508del/R1070W-CFTR P_O comparable to that of WT-CFTR (Liu et al., 2018), but a much lower P_O for temperature-corrected F508del-CFTR (Kopeikin et al., 2014; Liu et al., 2018; Wang et al., 2018) – note that single-channel conductance, γ, is unaffected by F508del and R1070W mutations (Dalemans et al., 1991; Thibodeau et al., 2010).

Plots of G_{CFTR} as a function of ρ for the rare-mutation panel give an overview of processing and gating/permeation defects caused by each missense mutation (Figure 5C). For instance, D579G-CFTR (orange open diamond at coordinates (0.35,41.5)) falls close to the WT-CFTR interpolation line, suggesting that the product of channel P_O and γ is not greatly affected by this mutation, and that the low short-circuit currents measured in FRT cells (Sosnay et al., 2013; Van Goor et al., 2014) are largely caused by the reduced membrane density. For G1244E (orange (0.75,7.2)) and S549N (blue (0.83,11)), likely altering the structure of P- and signature sequence loops, respectively, in site 2 measured ion channel function is much lower than would be expected given the high membrane density. Here low short-circuit currents (Sosnay et al., 2013) are likely due to gating defects. Most mutations give reduced membrane densities and a conductance that falls below the interpolation line, suggesting processing defects as well as some degree of impairment in gating/permeation for the molecules that do reach the membrane. We further illustrate the effect of acute treatment with VX-770 for mutations resulting in the strongest potentiation (fold-potentiation >20, Figure 5D). For many of these, data points for potentiated conductance fall above the interpolation line, suggesting that the product of P_O and γ is higher than measured for WT-CFTR in baseline-activated conditions.

Discussion

Many CFTR variants associated with CF, including the most common, F508del-CFTR, are characterized by both processing and functional defects. Rescue of either ion channel function or membrane density alone, is not enough for effective treatment of patients (Clancy et al., 2012; Flume et al., 2012). Therapies combining multiple correctors/potentiators are now

seen as most promising (Holguin, 2018). However, potentiators can negatively interfere with corrector action (Cholon et al., 2014; Meng et al., 2017; Veit et al., 2014). Furthermore, it has been suggested that maintaining a clear separation between correctors and potentiators does not usefully describe CFTR pharmacology (Rowe & Verkman, 2013). Practical implementation of distinct potentiator and corrector screens might have biased the search towards combination therapies, hampering discovery of modulators with true dual activity. All this highlights the potential impact of our assay, capable of simultaneously measuring pharmacological effects on membrane localization and on gating/permeation characteristics.

Our assay accurately detects changes in membrane density of CFTR, even when such changes are small and the heterogeneity among cells is large. Our assay can pick up a minute difference in membrane density between untreated and VX-809 treated HEK293 cells incubated at 37°C (Figure 2A left, Okiyoneda et al., 2013). The effect of the R1070W mutation on F508del-CFTR membrane density at 37°C is similarly small (Okiyoneda et al., 2013, Figure 2B left). In agreement with other studies (Cholon et al., 2014; Veit et al., 2014), we observed a small but significant shift in $\log_{10}\rho$ following chronic incubation with VX-770, consistent with the potentiator destabilizing F508del-CFTR at the membrane (Figure 2C left). We were also able to confirm that the membrane density of F508del-CFTR is increased at low temperature (Denning et al., 1992; Rennolds et al., 2008; Wang et al., 2008, Figure 2D). The effects of VX-809 treatment (He et al., 2013), R1070W rescue, and chronic treatment with VX-770 on membrane density are larger when combined with incubation at low temperature (Figure 2 right).

In addition to membrane density, our assay quantifies channel function,. Here, the assay is not optimized to measure high CFTR activities and some measurements hit the upper limit of its dynamic range (e.g. for WT-CFTR, Figs. 3 and 4, Supplementary Table S3). However, both the "I^- first" protocol (Langron et al., 2017), measuring the maximal rate of I^- entry ($\frac{\Delta[I^-]_{in}}{\Delta t}$) during CFTR activation, and "I^- last" protocol (Langron et al., 2018), estimating CFTR conductance by fitting quenching time course after steady-state activation is reached, can accurately quantify the low CFTR activities typically seen in mutants. While the "I^- last" protocol is unaffected by variability in signal transduction kinetics and better accounts for changing electrochemical potential gradients, the "I^- first" protocol allows faster data acquisition and less computationally intensive analysis. In line with results obtained with other techniques (e.g. Ussing chambers, high-throughput electrophysiology), our results show that

both G_{CFTR} (Sosnay et al., 2013; Van Goor et al., 2014) and $\frac{\Delta[I^-]_{in}}{\Delta t}$ (Billet et al., 2017; Van Goor et al., 2011) provide accurate estimates of CFTR activity.

Accurate quantification of low conductance values is advantageous in characterizing drug response by CFTR mutants, most of which have low residual activity. Our assay detects strong VX-770 potentiation for R347P-, N1303K- and H1085R-CFTR, genotypes giving no significant potentiation over baseline in the Ussing chamber study (Van Goor et al., 2014). While further studies on the functional effects of R347P and H1085R mutations are required, our results on N1303K are consistent with patch-clamp results (DeStefano et al., 2018). Such mutants should not be described as not "responding" to VX-770, as it is likely that they might benefit from therapies combining VX-770 with other modulators.

Empirical profiling of drug effects on the rare mutation panel can generate hypotheses on drug mechanism of action. Considering the sites of mutations resulting in the highest VX-770 efficacy (fold-potentiation >20, Figure 5D), these appear to link the ATP molecule bound at site 1 to regions close to the narrowest portion of the permeation pathway, thought to constitute the CFTR gate (El Hiani & Linsdell, 2010; Gao & Hwang, 2015), and positioned adjacent to the very recently identified VX-770 binding site (Liu et al., 2019) (Figure 6). It is interesting to note that ATP at site 1 contributes to stabilizing the opening transition state and even more the prehydrolytic O_1 state (Sorum et al., 2017). Similarly, binding of VX-770 results in an increased opening rate (Jih & Hwang, 2013) and a particularly stable O_1 state (Langron et al., 2018).

Among the highly VX-770-sensitive mutations, all those surrounding the ATP and NBD/TMD interface introduce charged side chains which would interact unfavourably with other close charges in the conformation observed for phosphorylated, ATP-bound human CFTR, carrying the open-state stabilizing E1371Q mutation, 6MSM (Zhang et al., 2018b): the aspartate replacing G1349, in the NBD2 signature sequence, with the γ-phosphate bound at site 1 (Bompadre et al., 2007); the lysine in place of N1303 in the NBD2 "socket", with R1358 in NBD2; the arginine replacing G178, in intracellular loop 1 (ICL1) with K254, E257 and R258 in ICL2 (Zhang et al., 2018b); the aspartate replacing H1054, in ICL4, with E543 in the NBD1 X-loop (He et al., 2008); the arginine in place of H1085, with R1048 in TM10 (for all listed pairs distances between α-carbons are below 10 Å). Mutations at these sites are likely to particularly destabilize the NBD-dimerized, ABC-canonical open channel conformation. It has been recently suggested that "undocking" of NBD1 from the TMDs might occur

physiologically (Sigoillot et al., 2019). VX-770 binding might allow channels to reach an alternative, particularly stable (Langron et al., 2018), open state, with a different conformation at the interface between site 1 and the TMDs, possibly comprising an undocked NBD1. Moreover, as the action of VX-770 has been found not to require ATP binding (Eckford et al., 2012), with the increase in opening rate unaffected by [ATP] (Jih & Hwang, 2013), the stability of this alternative open state (and of the transition state to reach it) might not be affected by bound ATP molecules.

The remaining two highly VX-770-sensitive mutations insert prolines, known to restrict backbone flexibility, in a region close to the CFTR gate. The R347P mutation, in TM6, affects a residue important for maintaining a stable conducting pathway (Cotten & Welsh, 1999; Cui et al., 2013; Kopeikin et al., 2010). The L927P mutation is in the unwound segment of TM8 (Corradi et al., 2018; Liu et al., 2017), underlying CFTR's unique channel function (Liu et al., 2017). The very low conductance measured after baseline activation in both these mutants, suggests that backbone flexibility at both these sites is required for channel opening and/or to maintain a conducting permeation pathway (Zhang et al., 2018b). VX-770 has been hypothesized to increase conformational flexibility of CFTR (Cholon et al., 2014) overall. It is possible that this increased flexibility might particularly concern the extracellular end of CFTR's transmembrane helices 8, 5, 4 and 6, surrounding the drug binding site, with VX-770 lubricating rearrangement of the helices and allowing adoption of the alternative open state described above.

Acute treatment with VX-770 is most effective on L927P channels, resulting in an ~80-fold potentiation. L927P is adjacent to A928, part of the VX-770 binding site (Liu et al., 2019). However, patients carrying the L927P mutation are not currently among the genotypes approved for VX-770 (alone or with corrector) treatment (Van Goor et al., 2014). Again, the L927P CFTR genotype could well benefit from therapies combining VX-770 with other modulators. Further investigation is required: patch-clamp recording of how the L927P-CFTR ion channel function is altered by binding of VX-770, and studies on chronic rather than acute treatment in native, patient-derived cells.

Conclusions and Implications

The main advantage of our assay consists in providing simultaneous measurements of ion channel function and membrane density. Currently available high throughput assays report on either CFTR membrane density or CFTR-mediated cellular conductance (G_{CFTR}). G_{CFTR} is

the product of 3 factors: the number of channels at the membrane (N), P_O, and γ ($G_{CFTR} = N \cdot P_O \cdot \gamma$). Being able to monitor how compounds or mutations affect both number of channels at the membrane and conductance can allow accurate deconvolution of effects on processing (altering N) from those influencing gating and permeation of the channel (affecting P_O and γ, respectively).

Describing each CF-causing mutation with two coordinates (ρ and G_{CFTR}) is a concise, informative way of characterizing mutations (e.g. Figure 5C) and the effects of CFTR modulators on them (e.g. Figure 5D). Implementing the assay at early stages (compound screening and structure-activity relationship studies) could better inform drug development, possibly enabling programmes seeking dual-activity (corrector/potentiator) modulators. In addition, assay results obtained with our rare mutation panel could give valuable insight relevant to patient stratification for clinical trial planning and/or could provide licensing authorities with useful material on which to base decisions on regulatory approval for treatment of patients with genotypes found only extremely rarely in the population (Ratner, 2017).

Finally, because CFTR plays an important role controlling fluid transport across several epithelia (Frizzell & Hanrahan, 2012; Saint-Criq & Gray, 2017), it has been implicated in a number of pathologies, including COPD (Solomon et al., 2017; Zhao et al., 2014), secretory diarrhoeas (Thiagarajah et al., 2015), polycystic kidney disease (Li et al., 2012) and others (Solymosi et al., 2013; Zhang et al., 2018a). It is likely that, given the complexity of CFTR folding and trafficking (Farinha & Canato, 2017; Lukacs & Verkman, 2012), many CFTR-targeting compounds will alter its cellular processing (Clunes et al., 2011), suggesting that the assay could also be usefully deployed in the development of novel CFTR-targeting drugs for other diseases, beyond CF.

Methods

Construction of the pIRES2-mCherry-YFPCFTR plasmid

The pIRES2-mCherry-YFPCFTR plasmid was obtained with two sequential subcloning steps. First, a 1.727kb region of pcDNA3.1-YFP-CFTR (Langron et al., 2017), containing the YFP-coding sequence, was subcloned into pIRES-eGFP-CFTR, a gift from David Gadsby (Rockefeller University), using the NheI and BlpI restriction sites. Subsequently a 0.737 kb region from pIRES2-mCherry-p53 deltaN (Lin et al., 2013) (Addgene), containing the mCherry-coding segment and part of the IRES, was subcloned into the pIRES-eGFP-YFPCFTR plasmid using the NotI and BmgBI/BtrI restriction sites. This resulted in the pIRES2-mCherry-YFPCFTR plasmid, with the IRES2 positioned between the two open reading frames for mCherry and YFP-CFTR.

HEK293 cell culture and transfection

HEK293 cells were maintained in Dulbecco's modified Eagle's medium (DMEM), supplemented with 2 mM L-glutamine, 100 U/mL penicillin and streptomycin, and 10% fetal bovine serum (all Life Technologies). Cells were seeded in poly-D-lysine-coated, black-walled 96-well plates (Costar, Fisher Scientific), and transiently transfected with the pIRES2-mCherry-YFPCFTR plasmid using Lipofectamine 2000 (Life Technologies). After transfection, cell plates were returned to the 37°C incubator for 24 hours. Prior to imaging plates were incubated for another 24 hours, at 37°C or 28°C, in 100 µL DMEM including DMSO (vehicle), 10 µM VX-809, or 10 µM VX-770 plus 10 µM VX-809 (Selleck Chemicals).

Image acquisition

Before imaging, cells were washed twice with 100 µL standard buffer (140 mM NaCl, 4.7 mM KCl, 1.2 mM MgCl2, 5 mM HEPES, 2.5 mM CaCl2,1mM glucose, pH 7.4). The ImageXpress Micro XLS (Molecular Devices), an automated inverted wide-field fluorescence microscope with a temperature-controlled chamber (set to 37°C or 28°C, as indicated), was used for image acquisition. Protocols for automated fluid additions, enabled by a robotic arm, were created using MetaXpress software (Molecular Devices). For imaging of YFP(H148Q/I152L)-CFTR, a 472 ± 30 nm excitation filter, and a 520 ± 35 nm emission filter were used. Excitation/emission filters at 531 ± 20 nm and 592 ± 20 nm were used for imaging of mCherry.

For localization of CFTR, a 60× objective was used to take 9 16-bit images per well of both fluorophores. To evaluate CFTR function, a 20× objective was used. Two 16-bit images of mCherry were taken, one at the start and one the end of the protocol. In addition, 16-bit images of the YFP fluorescence, were taken at an acquisition frequency of 0.5 Hz. For the I^- first protocol ((A), see below), after 20 s, 50 µL of 300 mM I^- buffer (300 mM NaI, 4.7 mM KCl, 1.2 mM $MgCl_2$, 5 mM HEPES, 2.5 mM $CaCl_2$,1mM glucose, pH 7.4) was added to the standard buffer, so that the final concentration of I^- in the extracellular medium was 100 mM. Another 40 s later, a further 50 µL of a 100 mM I^- buffer containing 40 µM forskolin (100 mM NaI, 4.7 mM KCl, 1.2 mM $MgCl_2$, 5 mM HEPES, 2.5 mM $CaCl_2$,1mM glucose, 40 µM forskolin, pH 7.4) was added, so that the final concentration of forskolin in the extracellular medium was 10 µM, while concentration of I^- and other components remained unaltered. For the I- last protocol ((B), below), after 20 s of imaging, CFTR was activated, in the absence of extracellular iodide, by addition of 50 µl standard buffer containing activating compounds (forskolin or forskolin + VX-770 both to reach final concentrations of 10 µM). After a further 230 s, by which time CFTR is assumed to be gating at steady state (Langron et al., 2018), 100 mM extracellular iodide (final concentration) was introduced by adding 50 µl of iodide buffer (as standard buffer with 140 mM NaCl replaced with 400 mM NaI). Images were taken for 40 more seconds. Activating compounds were also included in the second addition so as not to alter final extracellular concentrations.

Image analysis

Image analysis was automated using MATLAB mathematical computing software (MathWorks). Separate analysis protocols were implemented to estimate CFTR membrane density and ion channel function.

<u>CFTR membrane density</u>

First, mCherry images were binarized, and basic morphological operations (opening, closing, area opening, and dilation) were carried out to reduce noise. A distance transform with locally imposed minima was used to segment images by means of a watershed transformation and define cell boundaries. Cells were removed from analysis if they had an area of under 108 μm^2 or over 5400 μm^2, if they had a major axis length of less than 32.4 µm, if the area over perimeter was less than 25 or over 300, and if they were touching the edge of the image. A 1.08

µm band, 10 or 5 pixels wide (depending on the resolution of the image), within the border of each cell was defined as the membrane zone.

Background was selected by inverting the binarized and morphologically opened mCherry image, after which it was morphologically closed using a large structuring element to prevent cells from being selected as background. Average background intensity was then subtracted from each pixel, and the YFP and mCherry fluorescence intensity of each cell was normalized to the median YFP and mCherry fluorescence intensities of cells expressing WT-CFTR on the same plate. If the average normalized fluorescence intensity fell below 0 (due to low transfection efficiency and high background noise), cells were removed from analysis.

In order to estimate CFTR membrane density for each cell (defined as ρ, see Results), the average normalized YFP fluorescence intensity within the membrane zone was divided by the average normalized mCherry fluorescence over the entire cell.

$$\rho = \frac{F_{\text{YFP membrane}}}{F_{\text{mCherry cell}}}$$

CFTR ion channel function

For assessment of CFTR function, two different protocols were used. For both, cells were selected based on the mCherry fluorescence image that was taken at the beginning of the protocol.

(A) I^- first Protocol

The fluorescence at the time point before addition of I^- was used to normalize YFP fluorescence intensity. The concentration of I^- inside the cells ($[I^-]_{in}$) can be estimated with the following equation (Langron et al., 2017), in which the binding affinity for I^- (K_I) to YFP(H148Q/I152L) is 1.9 mM (Galietta et al., 2001a) and the normalized fluorescence intensity over time (*F(t)*) is determined experimentally.

$$[I^-]_{in} = K_I \frac{(1 - F(t))}{F(t)}$$

Data is collected every 2 seconds, so the change $[I^-]_{in}$ observed at each time point can be estimated and used to calculate the rate of I^- entry (in mM/s):

$$\frac{\Delta[I^-]_{in}}{\Delta t} = \frac{[I^-]_{in}(t) - [I^-]_{in}(t-1)}{2\ \text{s}}$$

The maximal observed rate of I^- entry is used as a measure of cellular anion conductance. To determine whether there was increased CFTR-mediated anion conductance, the maximal rate of I^- entry after addition of forskolin (which activates CFTR by cAMP dependent

phosphorylation), was compared to the maximal rate of I^- entry after addition of DMSO (vehicle, negative control).

(B) I^- last Protocol

CFTR activation (by addition of 10 μM forskolin with or without 10 μM VX-770, as indicated) was first allowed to reach steady state in the absence of I^- and quenching of YFP in the 40 s following extracellular I^- addition was measured. A simple mathematical model was used to fit observed fluorescence quenching, and estimate CFTR conductance as described (Langron et al., 2018). Briefly, the model includes four free parameters: CFTR conductance at steady-state (G_{CFTR}), membrane potential at steady-state, immediately prior to I^- addition (V_M), and conductance (G_{trans}) and time constant (τ_{trans}) of a transient, endogenous non-CFTR anion conductance. The values of the four parameters were estimated by minimizing the sum of squared residuals obtained by comparing the time course of the observed average fluorescence intensity within cells to the proportion of anion-free YFP chromophore predicted by the model (both normalized to the time point before I^- addition). However, when the quenching time course was too fast and did not provide enough information to uniquely identify all four parameters, the value of the latter two parameters was constrained to the average values obtained with negative controls, and only G_{CFTR} and V_M were estimated (Langron et al., 2018).

For both protocol (A) and (B) the value obtained from analysis of the observed YFP-CFTR fluorescence quenching ($\frac{\Delta[I^-]_{in}}{\Delta t}$ and G_{CFTR}, respectively) was corrected for variations in transfection efficiency, using the mean $F_{mCherry}$ within the cell selection normalized to $F_{mCherry}$ measured for WT in the same plate.

Data and Statistical analysis

The data and statistical analysis comply with the recommendations on experimental design and analysis in pharmacology (Curtis et al., 2018). Measurements of conductance from the rare mutation panel were repeated only on 3 or 4 independent samples (see Supplementary Tables S6 and S7). As demonstrated by the good correlation with published datasets (see Results) this is sufficient to give a first characterization of ion channel function, as is required for most screens. No statistical analysis was performed on this dataset.

Because ρ values approach a log-normal distribution, values were log transformed before performing statistical analysis, allowing parametric testing of the data. To determine whether the observed differences in ρ, $\frac{\Delta[I^-]_{in}}{\Delta t}$, or G_{CFTR} resulting from experimental manipulation and/or mutations were statistically significant, we performed either paired t-tests,

pairing conditions tested on the same plate, or independent t-tests. When required, either a Bonferroni or a Benjamini-Hochberg correction was applied to adjust for multiple comparisons. Data in graphs represent mean ± SEM, and the significance level was pre-specified as $\alpha = 0.05$. Statistical analysis was carried out using MATLAB (MathWorks), SigmaPlot (Systat Software), SPSS (IBM), or Excel (Microsoft).

Author Contributions

Experiments were conceived and designed by SP, EL and PV, after discussion with LDG and CH. SP and EL, with the help of ACS, CH and EH, carried out the molecular biology, ran the fluorescence assay acquisition and ran image analysis. SP, with the help of CH, implemented the image analysis protocols and the mathematical model in the MATLAB environment. Manuscript was written by SP, EL and PV. All authors read and commented on the final draft of the manuscript.

Acknowledgements

EL was supported by grant 15UCL04, funded by the Sparks charity and Cystic Fibrosis Trust. SP was supported by grant SRC005 funded by the Cystic Fibrosis Trust. CH was supported by EPSRC grant EP/F500351/1, and ACS was awarded a British Pharmacological Society Vacation Studentship. We thank Dr William Andrews, Central Molecular Laboratory, UCL for help with molecular biology.

Conflict of interest declaration

The authors declare no conflicts of interest.

References

Billet A, Froux L, Hanrahan JW, & Becq F (2017). Development of Automated Patch Clamp Technique to Investigate CFTR Chloride Channel Function. Front Pharmacol 8.

Bompadre SG, Sohma Y, Li M, & Hwang T-C (2007). G551D and G1349D, Two CF-associated Mutations in the Signature Sequences of CFTR, Exhibit Distinct Gating Defects. J Gen Physiol 129**:** 285-298.

Cholon DM, Quinney NL, Fulcher ML, Esther CR, Das J, Dokholyan NV, *et al.* (2014). Potentiator ivacaftor abrogates pharmacological correction of deltaF508 CFTR in cystic fibrosis. Sci Transl Med 6**:** 246ra296.

Clancy JP, Rowe SM, Accurso FJ, Aitken ML, Amin RS, Ashlock MA, *et al.* (2012). Results of a phase IIa study of VX-809, an investigational CFTR corrector compound, in subjects with cystic fibrosis homozygous for the F508del-CFTR mutation. Thorax 67**:** 12-18.

Clunes LA, Davies CM, Coakley RD, Aleksandrov AA, Henderson AG, Zeman KL, *et al.* (2011). Cigarette smoke exposure induces CFTR internalization and insolubility, leading to airway surface liquid dehydration. The FASEB Journal.

Corradi V, Gu R-X, Vergani P, & Tieleman DP (2018). Structure of Transmembrane Helix 8 and Possible Membrane Defects in CFTR. Biophys J 114**:** 1751-1754.

Cotten JF, & Welsh MJ (1999). Cystic Fibrosis-associated Mutations at Arginine 347 Alter the Pore Architecture of CFTR. Evidence for disruption of a salt bridge. J Biol Chem 274**:** 5429-5435.

Csanády L, Vergani P, & Gadsby DC (2019). STRUCTURE, GATING, AND REGULATION OF THE CFTR ANION CHANNEL. Physiol Rev 99**:** 707-738.

Cui G, Freeman CS, Knotts T, Prince CZ, Kuang C, & McCarty NA (2013). Two Salt Bridges Differentially Contribute to the Maintenance of Cystic Fibrosis Transmembrane Conductance Regulator (CFTR) Channel Function. J Biol Chem 288**:** 20758-20767.

Curtis MJ, Alexander S, Cirino G, Docherty JR, George CH, Giembycz MA, *et al.* (2018). Experimental design and analysis and their reporting II: updated and simplified guidance for authors and peer reviewers. Br J Pharmacol 175**:** 987-993.

Dalemans W, Barbry P, Champigny G, Jallat S, Jallat S, Dott K, *et al.* (1991). Altered chloride ion channel kinetics associated with the [Delta]F508 cystic fibrosis mutation. Nature 354**:** 526-528.

Davies JC, Moskowitz SM, Brown C, Horsley A, Mall MA, McKone EF, *et al.* (2018). VX-659–Tezacaftor–Ivacaftor in Patients with Cystic Fibrosis and One or Two Phe508del Alleles. N Engl J Med 379**:** 1599-1611.

Denning GM, Anderson MP, Amara JF, Marshall J, Smith AE, & Welsh MJ (1992). Processing of mutant cystic fibrosis transmembrane conductance regulator is temperature-sensitive. Nature 358**:** 761-764.

DeStefano S, Gees M, & Hwang T-C (2018). Physiological and pharmacological characterization of the N1303K mutant CFTR. Journal of Cystic Fibrosis.

Eckford PDW, Li C, Ramjeesingh M, & Bear CE (2012). Cystic Fibrosis Transmembrane Conductance Regulator (CFTR) Potentiator VX-770 (Ivacaftor) Opens the Defective Channel Gate of Mutant CFTR in a Phosphorylation-dependent but ATP-independent Manner. J Biol Chem 287**:** 36639-36649.

El Hiani Y, & Linsdell P (2010). Changes in Accessibility of Cytoplasmic Substances to the Pore Associated with Activation of the Cystic Fibrosis Transmembrane Conductance Regulator Chloride Channel. J Biol Chem 285**:** 32126-32140.

Elborn JS (2016). Cystic fibrosis. The Lancet 388**:** 2519-2531.

Farinha CM, & Canato S (2017). From the endoplasmic reticulum to the plasma membrane: mechanisms of CFTR folding and trafficking. cell Mol Life Sci 74**:** 39-55.

Farinha CM, King-Underwood J, Sousa M, Correia Ana R, Henriques Barbara J, Roxo-Rosa M, *et al.* (2013). Revertants, Low Temperature, and Correctors Reveal the Mechanism of F508del-CFTR Rescue by VX-809 and Suggest Multiple Agents for Full Correction. Chem Biol 20**:** 943-955.

Flume PA, Liou TG, Borowitz DS, Li H, Yen K, Ordoñez CL, *et al.* (2012). Ivacaftor in subjects with cystic fibrosis who are homozygous for the f508del-cftr mutation. Chest 142**:** 718-724.

Frizzell RA, & Hanrahan JW (2012). Physiology of Epithelial Chloride and Fluid Secretion. Cold Spring Harb Perspect Med 2.

Galietta L, Haggie P, & Verkman A (2001a). Green fluorescent protein-based halide indicators with improved chloride and iodide affinities. FEBS Lett 499**:** 220-224.

Galietta L, Jayaraman S, & Verkman A (2001b). Cell-based assay for high-throughput quantitative screening of CFTR chloride transport agonists. Am J Physiol Cell Physiol 281**:** C1734-C1742.

Gao X, & Hwang T-C (2015). Localizing a gate in CFTR. Proceedings of the National Academy of Sciences of the United States of America 112**:** 2461-2466.

Gentzsch M, & Mall MA (2018). Ion Channel Modulators in Cystic Fibrosis. Chest 154**:** 383-393.

He L, Aleksandrov AA, Serohijos AWR, Hegedus T, Aleksandrov LA, Cui L, *et al.* (2008). Multiple Membrane-Cytoplasmic Domain Contacts in the Cystic Fibrosis Transmembrane Conductance Regulator (CFTR) Mediate Regulation of Channel Gating. J Biol Chem 283**:** 26383-26390.

He L, Kota P, Aleksandrov AA, Cui L, Jensen T, Dokholyan NV, *et al.* (2013). Correctors of deltaF508 CFTR restore global conformational maturation without thermally stabilizing the mutant protein. FASEB J 27**:** 536-545.

Holguin F (2018). Triple CFTR Modulator Therapy for Cystic Fibrosis. N Engl J Med 379**:** 1671-1672.

Jih K-Y, & Hwang T-C (2013). Vx-770 potentiates CFTR function by promoting decoupling between the gating cycle and ATP hydrolysis cycle. Proceedings of the National Academy of Sciences of the United States of America 110**:** 4404-4409.

Keating D, Marigowda G, Burr L, Daines C, Mall MA, McKone EF, *et al.* (2018). VX-445–Tezacaftor–Ivacaftor in Patients with Cystic Fibrosis and One or Two Phe508del Alleles. New England Journal of Medicine 379**:** 1612-1620.

Kopeikin Z, Sohma Y, Li M, & Hwang T-C (2010). On the mechanism of CFTR inhibition by a thiazolidinone derivative. J Gen Physiol 136**:** 659.

Kopeikin Z, Yuksek Z, Yang HY, & Bompadre SG (2014). Combined effects of VX-770 and VX-809 on several functional abnormalities of F508del-CFTR channels. Journal of Cystic Fibrosis 13**:** 508-514.

Langron E, Prins S, & Vergani P (2018). Potentiation of the cystic fibrosis transmembrane conductance regulator by VX-770 involves stabilization of the pre-hydrolytic, O1 state. Br J Pharmacol 175**:** 3990-4002.

Langron E, Simone MI, Delalande CMS, Reymond J-L, Selwood DL, & Vergani P (2017). Improved fluorescence assays to measure the defects associated with F508del-CFTR allow identification of new active compounds. Br J Pharmacol 174**:** 525-539.

Li H, Yang W, Mendes F, Amaral MD, & Sheppard DN (2012). Impact of the cystic fibrosis mutation F508del-CFTR on renal cyst formation and growth. Am J Physiol Renal Physiol 303**:** F1176-F1186.

Lin S-C, Karoly ED, & Taatjes DJ (2013). The human ΔNp53 isoform triggers metabolic and gene expression changes that activate mTOR and alter mitochondrial function. Aging Cell 12**:** 863-872.

Liu F, Zhang Z, Csanády L, Gadsby DC, & Chen J (2017). Molecular Structure of the Human CFTR Ion Channel. Cell 169**:** 85-95.e88.

Liu F, Zhang Z, Levit A, Levring J, Touhara KK, Shoichet BK, *et al.* (2019). Structural identification of a hotspot on CFTR for potentiation. Science 364**:** 1184-1188.

Liu J, Bihler H, Farinha CM, Awatade NT, Romão AM, Mercadante D, *et al.* (2018). Partial rescue of F508del-cystic fibrosis transmembrane conductance regulator channel gating with modest improvement of protein processing, but not stability, by a dual-acting small molecule. Br J Pharmacol 175**:** 1017-1038.

Lukacs GL, & Verkman AS (2012). CFTR: folding, misfolding and correcting the [delta]F508 conformational defect. Trends Mol Med 18**:** 81-91.

Ma T, Vetrivel L, Yang H, Pedemonte N, Zegarra-Moran O, Galietta LJV, *et al.* (2002). High-affinity Activators of Cystic Fibrosis Transmembrane Conductance Regulator (CFTR) Chloride Conductance Identified by High-throughput Screening. J Biol Chem 277**:** 37235-37241.

Meng X, Wang Y, Wang X, Wrennall JA, Rimington TL, Li H, *et al.* (2017). Two Small Molecules Restore Stability to a Subpopulation of the Cystic Fibrosis Transmembrane Conductance Regulator with the Predominant Disease-causing Mutation. J Biol Chem 292**:** 3706-3719.

Okiyoneda T, Veit G, Dekkers JF, Bagdany M, Soya N, Xu H, *et al.* (2013). Mechanism-based corrector combination restores deltaF508-CFTR folding and function. Nat Chem Biol 9**:** 444-454.

Pedemonte N, Lukacs GL, Du K, Caci E, Zegarra-Moran O, Galietta LJV, *et al.* (2005a). Small-molecule correctors of defective {Delta}F508-CFTR cellular processing identified by high-throughput screening. J Clin Invest 115**:** 2564-2571.

Pedemonte N, Sonawane ND, Taddei A, Hu J, Zegarra-Moran O, Suen YF, *et al.* (2005b). Phenylglycine and Sulfonamide Correctors of Defective {Delta}F508 and G551D Cystic Fibrosis Transmembrane Conductance Regulator Chloride-Channel Gating. Mol Pharmacol 67**:** 1797-1807.

Ratner M (2017). FDA deems in vitro data on mutations sufficient to expand cystic fibrosis drug label. Nature Biotechnology 35**:** 606.

Rennolds J, Boyaka PN, Bellis SL, & Cormet-Boyaka E (2008). Low temperature induces the delivery of mature and immature CFTR to the plasma membrane. Biochem Biophys Res Commun 366**:** 1025-1029.

Riordan JR, Rommens JM, Kerem B, Alon N, Rozmahel R, Grzelczak Z, *et al.* (1989). Identification of the cystic fibrosis gene: cloning and characterization of complementary DNA. Science 245**:** 1066-1073.

Rommens JM, Iannuzzi MC, Kerem B-s, Drumm ML, Melmer G, Dean M, *et al.* (1989). Identification of the Cystic Fibrosis Gene: Chromosome Walking and Jumping. Science 245**:** 1059-1065.

Rowe SM, & Verkman AS (2013). Cystic Fibrosis Transmembrane Regulator Correctors and Potentiators. Cold Spring Harb Perspect Med 3**:** a009761.

Saint-Criq V, & Gray MA (2017). Role of CFTR in epithelial physiology. Cellular and Molecular Life Sciences 74**:** 93-115.

Shaner NC, Campbell RE, Steinbach PA, Giepmans BNG, Palmer AE, & Tsien RY (2004). Improved monomeric red, orange and yellow fluorescent proteins derived from Discosoma sp. red fluorescent protein. Nat Biotechnol 22**:** 1567.

Sigoillot M, Overtus M, Grodecka M, Scholl D, Garcia-Pino A, Laeremans T, *et al.* (2019). Domain-interface dynamics of CFTR revealed by stabilizing nanobodies. Nature Communications 10**:** 2636.

Solomon GM, Fu L, Rowe SM, & Collawn JF (2017). The therapeutic potential of CFTR modulators for COPD and other airway diseases. Current Opinion in Pharmacology 34**:** 132-139.

Solymosi EA, Kaestle-Gembardt SM, Vadász I, Wang L, Neye N, Chupin CJA, *et al.* (2013). Chloride transport-driven alveolar fluid secretion is a major contributor to cardiogenic lung edema. Proceedings of the National Academy of Sciences of the United States of America 110**:** E2308-E2316.

Sorum B, Töröcsik B, & Csanády L (2017). Asymmetry of movements in CFTR's two ATP sites during pore opening serves their distinct functions. eLife 6**:** e29013.

Sosnay PR, Siklosi KR, Van Goor F, Kaniecki K, Yu H, Sharma N, *et al.* (2013). Defining the disease liability of variants in the cystic fibrosis transmembrane conductance regulator gene. Nat Genet 45**:** 1160-1167.

Thiagarajah JR, Donowitz M, & Verkman AS (2015). Secretory diarrhoea: mechanisms and emerging therapies. Nat Rev Gastroenterol Hepatol 12**:** 446-457.

Thibodeau PH, Richardson JM, Wang W, Millen L, Watson J, Mendoza JL, *et al.* (2010). The Cystic Fibrosis-causing Mutation deltaF508 Affects Multiple Steps in Cystic Fibrosis Transmembrane Conductance Regulator Biogenesis. J Biol Chem 285**:** 35825-35835.

Van Goor F, Hadida S, Grootenhuis PDJ, Burton B, Cao D, Neuberger T, *et al.* (2009). Rescue of CF airway epithelial cell function in vitro by a CFTR potentiator, VX-770. Proceedings of the National Academy of Sciences of the United States of America 106**:** 18825-18830.

Van Goor F, Hadida S, Grootenhuis PDJ, Burton B, Stack JH, Straley KS, *et al.* (2011). Correction of the F508del-CFTR protein processing defect in vitro by the investigational drug VX-809. Proceedings of the National Academy of Sciences of the United States of America 108**:** 18843-18848.

Van Goor F, Straley KS, Cao D, Gonzalez J, Hadida S, Hazlewood A, *et al.* (2006). Rescue of {Delta}F508-CFTR trafficking and gating in human cystic fibrosis airway primary cultures by small molecules. Am J Physiol Lung Cell Mol Physiol 290**:** L1117-1130.

Van Goor F, Yu H, Burton B, & Hoffman BJ (2014). Effect of ivacaftor on CFTR forms with missense mutations associated with defects in protein processing or function. J Cyst Fibros 13**:** 29-36.

Veit G, Avramescu RG, Perdomo D, Phuan P-W, Bagdany M, Apaja PM, *et al.* (2014). Some gating potentiators, including VX-770, diminish F508del-CFTR functional expression. Sci Transl Med 6**:** 246ra297.

Wainwright CE, Elborn JS, Ramsey BW, Marigowda G, Huang X, Cipolli M, *et al.* (2015). Lumacaftor–Ivacaftor in Patients with Cystic Fibrosis Homozygous for Phe508del CFTR. N Engl J Med 373**:** 220-231.

Wang X, Koulov AV, Kellner WA, Riordan JR, & Balch WE (2008). Chemical and Biological Folding Contribute to Temperature-Sensitive ΔF508 CFTR Trafficking. Traffic 9**:** 1878-1893.

Wang Y, Cai Z, Gosling M, & Sheppard DN (2018). Potentiation of the cystic fibrosis transmembrane conductance regulator Cl− channel by ivacaftor is temperature independent. American Journal of Physiology-Lung Cellular and Molecular Physiology 315**:** L846-L857.

Yang H, Shelat AA, Guy RK, Gopinath VS, Ma T, Du K, *et al.* (2003). Nanomolar Affinity Small Molecule Correctors of Defective {Delta}F508-CFTR Chloride Channel Gating. J Biol Chem 278**:** 35079-35085.

Yu H, Burton B, Huang C-J, Worley J, Cao D, Johnson Jr JP, *et al.* (2012). Ivacaftor potentiation of multiple CFTR channels with gating mutations. J Cyst Fibros 11**:** 237-245.

Zhang J, Wang Y, Jiang X, & Chan HC (2018a). Cystic fibrosis transmembrane conductance regulator—emerging regulator of cancer. Cellular and Molecular Life Sciences 75**:** 1737-1756.

Zhang Z, Liu F, & Chen J (2018b). Molecular structure of the ATP-bound, phosphorylated human CFTR. Proceedings of the National Academy of Sciences of the United States of America.

Zhao R, Liang X, Zhao M, Liu S-L, Huang Y, Idell S, *et al.* (2014). Correlation of Apical Fluid-Regulating Channel Proteins with Lung Function in Human COPD Lungs. PLOS ONE 9**:** e109725.

Figures and figure legends

Figure 1

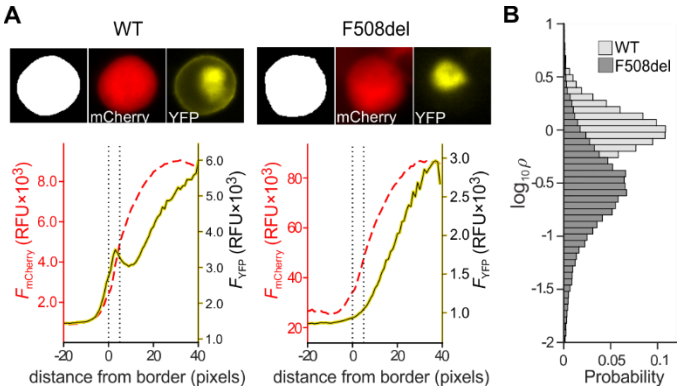

Image analysis to quantify CFTR membrane density (**A**) Image analysis of individual representative HEK293 cells transfected with pIRES2-mCherry-YFP-WT-CFTR (left), and pIRES2-mCherry-YFP-F508del-CFTR (right). Upper panels: boundary delimiting cell (white) from non-cell (black) is obtained from mCherry image (centre). CFTR cellular localization is obtained from YFP image (right). Lower panels: average mCherry fluorescence intensity (F_{mCherry}, red dashed line), and average YFP fluorescence intensity (F_{YFP}, solid yellow line), as a function of the distance from cell border. Membrane density is defined as

$$\rho = \frac{F_{\text{YFP membrane}}}{F_{\text{mCherry cell}}}$$

where $F_{\text{YFP membrane}}$ is the average fluorescence intensity within the 'membrane' zone, set between 0 and 5 pixels from the cell border. (**B**) Probability density distribution of $\log_{10}\rho$ for cells expressing YFP-WT-CFTR (light grey), and YFP-F508del-CFTR (dark grey), incubated at 37 °C. For the WT cell shown, $\rho = 1.60$; for the F508del cell, $\rho = 0.25$.

Figure 2

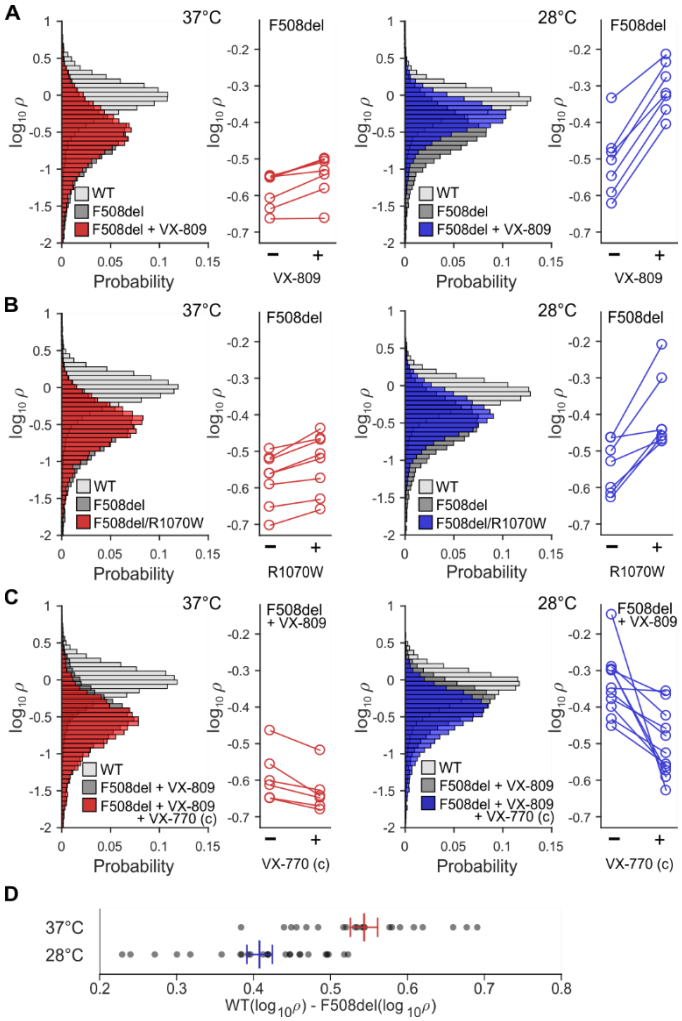

Monitoring CFTR membrane density ($\log_{10}\rho$) in HEK293 cells expressing WT-CFTR, F508del-CFTR, or F508del/R1070W-CFTR. Effects of chronic treatment with 10 µM VX-809 (**A**), R1070W rescue (**B**), and chronic treatment with 10 µM VX-809 + 10 µM VX-770 (**C**), on $\log_{10}\rho$ at 37°C (left, red) and 28°C (right, blue). Conditions of final incubation were maintained during image acquisition. The probability distributions in the panels on the left, contain $\log_{10}\rho$ measurements from thousands of cells, pooled from all experiments. For statistical analysis, mean $\log_{10}\rho$ values determined in independent experiments, and paired per plate, were used (displayed in panels on the right) (**D**) Before imaging, plates were incubated at 37°C, or 28°C for 24 hours. For each plate, the difference between mean $\log_{10}\rho$ for WT-CFTR and F508del-CFTR was calculated (WT($\log_{10}\rho$) - F508del($\log_{10}\rho$), grey dots). Red (37°C) and blue (28°C) lines show mean ± SEM, calculated from 21(37°C) and 25(28°C) within-plate difference estimates.

Figure 3

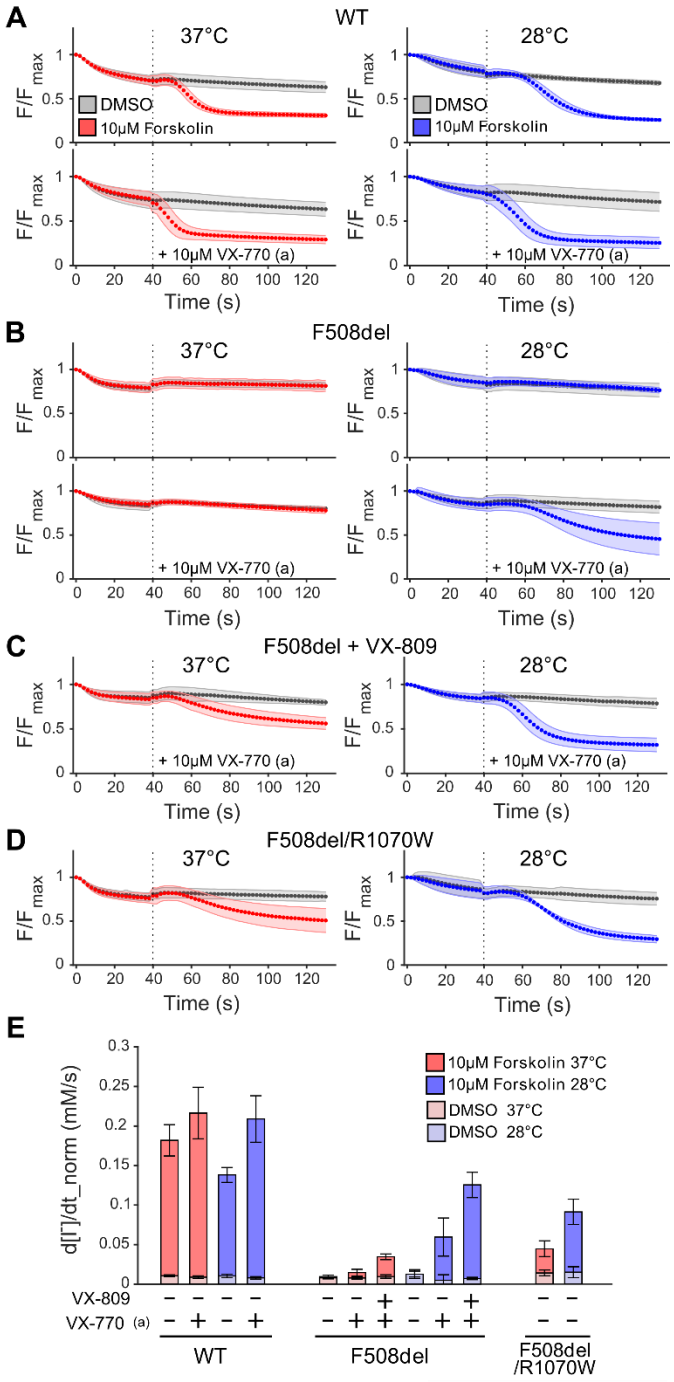

Monitoring CFTR ion channel function. (**A-D**) Quenching of YFP fluorescence in HEK293 cells expressing WT-CFTR (**A**), F508del-CFTR chronically (24 h) treated with DMSO (**B**) or with VX-809 (**C**), and R1070W/F508del-CFTR (**D**). For more information on statistical analysis see Supplementary Tables S2 and S3. Prior to imaging plates were incubated for 24 hours, at 37°C (left panels, red) or 28°C (right panels, blue). This final incubation temperature was maintained throughout image acquisition. At time point 0 s I^- was added to the extracellular medium. At 40 s forskolin and, where indicated, VX-770 (acute, a) was added (dotted line),

both to a final concentration of 10 μM. The fluorescence before addition of I^- (F_{max}), was used to normalize YFP fluorescence intensity. (**E**) The maximal rate of I^- entry (d[I^-]/dt_norm) is used to summarize CFTR function for genotypes and conditions shown in (**A**-**D**).

890 **Figure 4**

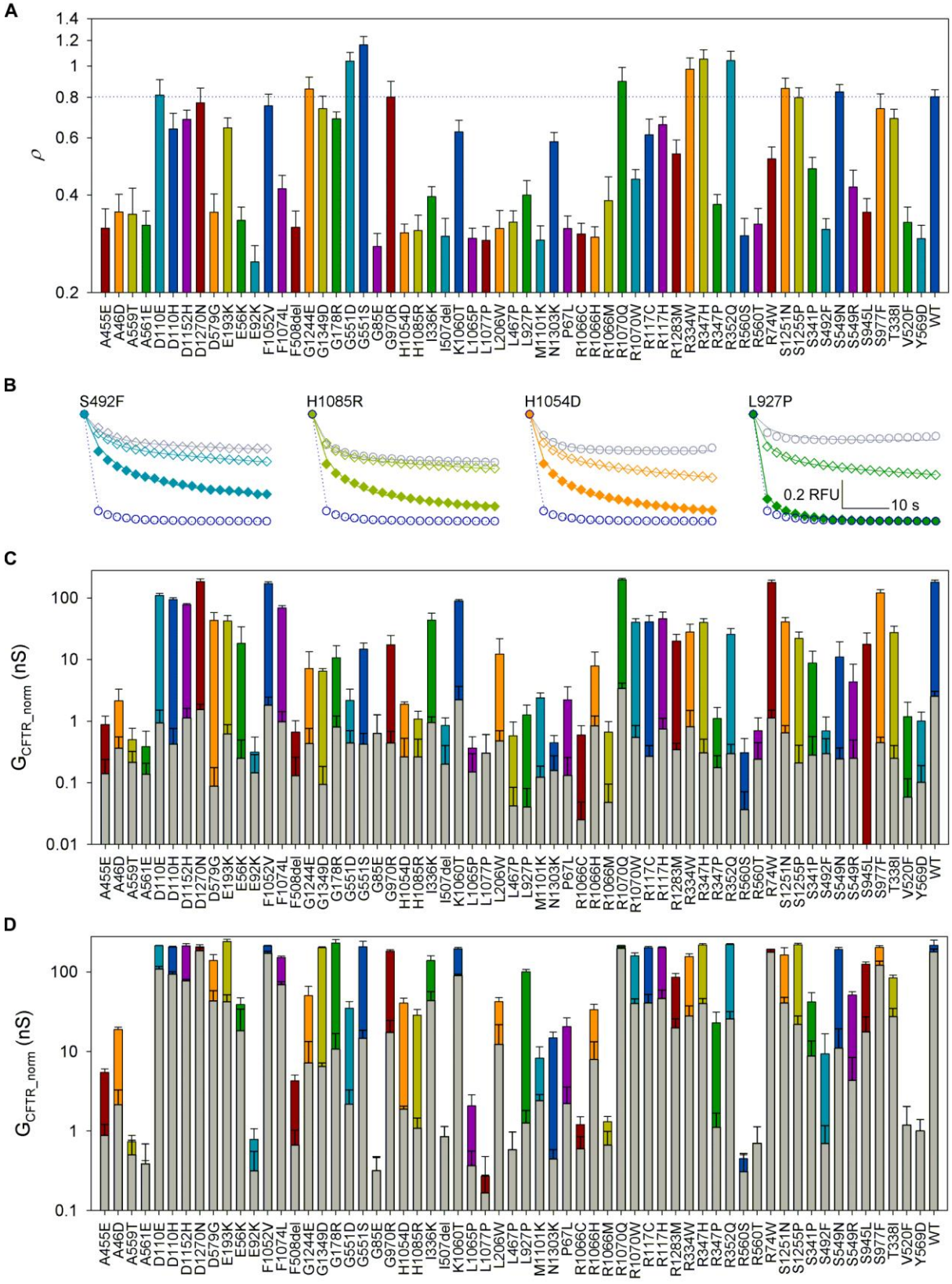
A
ρ
1.4
1.2
1
0.8
0.6
0.4
0.2
A455E A46D A559T A561E D110E D110H D1152H D1270N D579G E193K E56K E92K F1052V F1074L F508del G1244E G1349D G178R G551D G551S G85E G970R H1054D H1085R I336K I507del K1060T L1065P L1077P L206W L467P L927P M1101K N1303K P67L R1066C R1066H R1066M R1070Q R1070W R117C R117H R1283M R334W R347H R347P R352Q R560S R560T R74W S1251N S1255P S341P S492F S549N S549R S945L S977F T338I V520F Y569D WT
B
S492F
H1085R
H1054D
L927P
0.2 RFU
10 s
C
G_{CFTR_norm} (nS)
100
10
1
0.1
0.01
D
G_{CFTR_norm} (nS)
100
10
1
0.1

Rare CF-mutation profiling. (**A**) Mean ρ ($n \geq 9$) of all mutations in the panel. Dotted line indicates mean ρ for WT-CFTR. For ρ distributions, mean ρ and n values for each mutant see Supplementary Figure S5 and Supplementary Table S4. (**B**) Observed YFP quenching time course in the presence of DMSO (grey circles) or 10 μM forskolin (empty coloured diamonds), or 10 μM forskolin + acute 10 μM VX-770 (filled coloured diamonds) for selected mutations. Solid lines show predicted change in proportion of anion-free YFP. For estimated parameters G_{CFTR}, V_M, G_{trans} and τ_{trans} see Supplementary Table S8. WT-CFTR quenching in 10 μM forskolin (dark blue empty circles and dotted line) shown for comparison. (**C**) CFTR conductance of rare mutation panel after activation with 10 μM forskolin (coloured bars) or vehicle control (DMSO, grey bars). $n \geq 3$. G_{CFTR} obtained from fitting of quenching time-course for each mutant was normalized using the mean within cell mCherry fluorescence for that mutant, measured with respect to the corresponding metric obtained for WT-CFTR on the same plate. (**D**) Potentiation of rare mutation panel by VX-770. Grey bars show values following activation with 10 μM forskolin alone, coloured bars with further addition of acute 10 μM VX-770. For more information on statistical analysis of quenching data see Supplementary Tables S6 and S7.

Figure 5

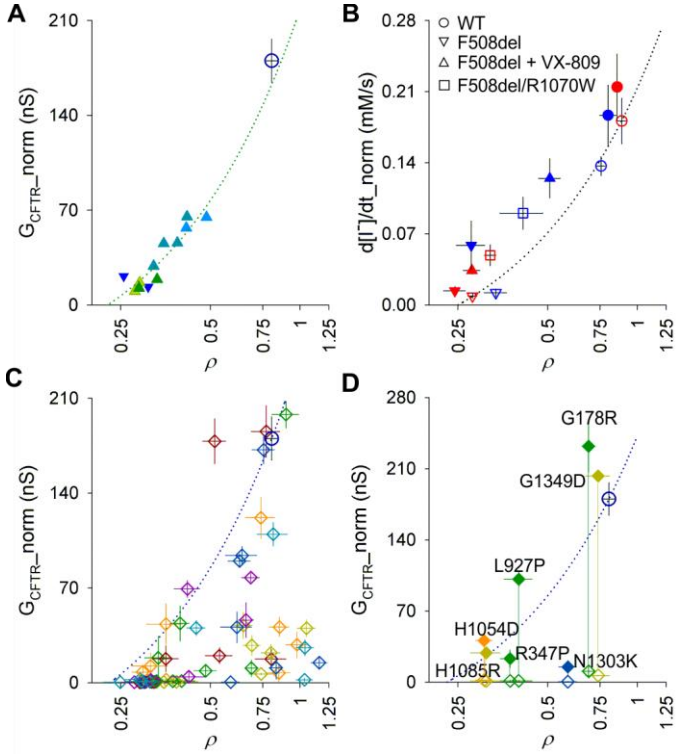

Investigating permeation/gating characteristics. (**A**) Relationship between normalized CFTR conductance and membrane density in cells expressing F508del-CFTR with no correction (blue ∇) or incubated with increasing concentrations of VX-809 (1 nM to 10 μM, green to light blue Δ), all after activation with 10 μM forskolin and acute potentiation with 10 μM VX-770. F508del-CFTR incubation and measurements were at 28°C. Green dotted line shows linear regression using only F508del-CFTR data points on graph (slope = 281.7, constant = -63.7, resulting in an x-axis intercept at $\rho = 0.23$). Mean value for WT-CFTR activated with 10 μM forskolin alone is shown for reference (from (**C**), large dark blue empty circle). (**B**) Relationship between maximal rate of I^- influx and ρ in HEK293 cells expressing WT-CFTR, F508del-CFTR, and F508del/R1070W-CFTR, at 37°C (red) and 28°C (blue). 10 μM forskolin was used to activate CFTR. Empty symbols indicate activation with forskolin alone. Solid symbols indicate further acute potentiation with 10 μM VX-770. Dotted line: linear interpolation between data obtained at 37°C for uncorrected F508del-CFTR and WT-CFTR, both without acute VX-770 potentiation; slope = 0.284, constant = -0.071, resulting in an x-axis intercept at $\rho = 0.25$. (**C**) Relationship between baseline G_{CFTR_norm} (10 μM forskolin) and ρ for rare mutation panel. Colours as in Figure 4. WT-CFTR is highlighted as a large, dark blue, empty circle. The dark blue dotted line (slope = 314.1, constant= -72.3) shows linear

interpolation between WT data points and x-axis intercept set at ρ =0.23, as obtained in (**A**). (**D**) Mutants with largest fold potentiation by VX-770 (ratio between conductance obtained in 10 μM forskolin + 10 μM VX-770 over that in 10 μM forskolin alone > 20). Empty diamonds indicate baseline activation with 10 μM forskolin alone, solid diamonds indicate activation following acute potentiation with 10 μM forskolin + 10 μM VX-770.

Figure 6

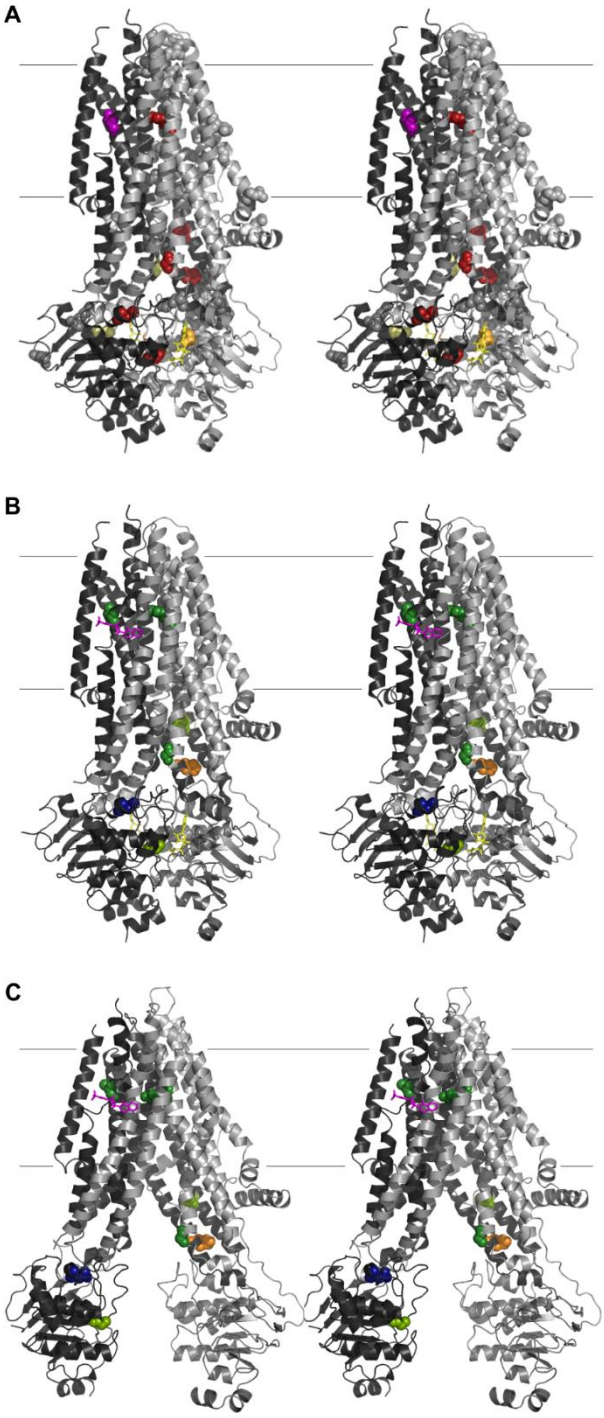

Mapping VX-770 sensitivity on cryo-EM structures. (**A**) Cartoon representation (cross-eye stereo) of phosphorylated, ATP-bound human CFTR, 6MSM (Zhang et al., 2018b), with sites of missense mutations in panel highlighted as spheres. Colours indicate degree of VX-770-potentiaton (fold potentiation, F < 5, grey; 5 < F < 10, white; 10 < F < 15, light yellow; 15 < F < 20, orange; 20 < F < 50, red; F > 50 purple). TMD1-NBD1 in light grey; TMD2-NBD2 in dark grey. Fine horizontal lines show approximate position of membrane boundary. (**B**) Only

positions with most efficacious VX-770 potentiation are shown. Magenta sticks show position of bound VX-770 in 6O2P structure (Liu et al., 2019). Mutation-site residues are colour-coded as in Fig. 4 (moving from cytosol to extracellular): G1349, light green; N1303, dark blue; H1054, orange; G178, forest; H1085, light green; R347, forest right; L927 forest left. (**C**) Orientation as in (**A,B**) but using atom coordinates of dephosphorylated human CFTR, 5UAK (Liu et al., 2017).